Research Square

Preprints are preliminary reports that have not undergone peer review.
They should not be considered conclusive, used to inform clinical practice,
or referenced by the media as validated information.

Internal Defect Monitoring System Design for Aluminum Conductor Composite Cores Using a Magnetic-Coating Interlayer in Power Transmission Lines

Young-Dae Shim
Georgia Institute of Technology
Changhyeon Kim
Sungkyunkwan University
Jihun Kim
Sungkyunkwan University
Eun-Ho Lee
e.h.lee@skku.edu

Sungkyunkwan University

Research Article

Keywords:

Posted Date: March 25th, 2026

DOI: https://doi.org/10.21203/rs.3.rs-9123365/v1

License: This work is licensed under a Creative Commons Attribution 4.0 International License.
Read Full License

Additional Declarations: No competing interests reported.

Internal Defect Monitoring System Design for Aluminum Conductor Composite Cores Using a Magnetic-Coating Interlayer in Power Transmission Lines

Abstract

As power grids demand higher capacity and efficiency, aluminum conductor composite core (ACCC) cables have become increasingly important. However, the reliability of these conductors depends on the structural integrity of their internal composite cores, where hidden defects are difficult to detect due to electromagnetic shielding by surrounding aluminum conductors. This paper proposes a magnetic coating interlayer integrated into the composite core to enable electromagnetic detection of internal defects. The coating enhances the magnetic permeability of the core, improving sensitivity to defect-induced field variations measured by an external sensor. The sensor configuration was optimized through electromagnetic analysis to maximize detection capability. The magnetic coating, composed of epoxy resin and magnetic particles, was further optimized by evaluating signal-to-noise ratio (SNR) and adhesion strength. Numerical simulations, cross-cut adhesion tests, and Pareto analysis were conducted to identify the optimal balance between sensitivity and durability. Experimental validation using a coated composite core embedded in an aluminum pipe confirmed the effectiveness of the proposed method. This technique provides a practical solution for both pre-installation and in-service defect monitoring of ACCC composite cores.

1. Introduction

Owing to the increase in the consumption of electrical energy, an increase in the capacity for electricity transmission is required. Most of the widely used conductors for power transmission lines are aluminum conductor steel reinforced (ACSR) conductors or all aluminum alloy conductors

(AAACs), which were developed in the early 1900s (Lequien et al., 2021). These conductors have been replaced by aluminum conductor steel supported (ACSS) conductors, in which the material of the conductor part has been changed from drawn aluminum to annealed aluminum (Jalilian et al., 2024). This increases the efficiency of power delivery owing to the decrease in conductor resistance. Moreover, the steel strands in ACSR conductors mostly support the weight of the power line in high operating temperatures, which results in excessive sag compared with ACSS conductors, in which aluminum and steel strands support the weight together. Nevertheless, the steel support in ACSS conductors cannot prevent the sag induced by Joule heating and thermal expansion caused by the significant consumption of electricity today. This problem further deteriorates in the summer season: the high atmospheric temperature strongly affects the thermal expansion of conductors, and along with the high demand for electricity, this can cause blackouts in the power grid (Alawar et al., 2005; Mahin et al., 2022). The aluminum conductor composite core (ACCC) was designed and developed to solve the problems of current capacity and sag. The ACCC is a new type of transmission conductor that prevents sagging by replacing the steel wire core with a low-density carbon fiber-reinforced plastic (CFRP). The ACCC has advantages over conventional conductors, such as ACSR or ACSS, in terms of current capacity and line loss. A larger cross-section of aluminum is included because of the lightweight property of the core. This decreases the resistance of the power line and simultaneously reduces Joule heating and temperature. Furthermore, existing grids can be upgraded without replacing the towers owing to its high current capacity. For newly constructed grids, the use of ACCCs enables the length of the tower span to be increased. However, although the composite core has low density and high-strength mechanical properties, its brittleness causes defects during the manufacturing or transportation of transmission conductors. Conductors that are excessively bent around wooden drums used for transportation generate axial tensile and compressive stresses on the composite core (Burks et al., 2010). Stress is concentrated at the interface of dissimilar materials because of the difference in the elastic modulus. CFRP composites are inherently weak to compressive loads. The fiber bands in the matrix buckle under compression, and the fibers break through kinking and bending (Larsson et al., 2023). This generates a crack on the CFRP surface when the ACCC wires are wound on drums with a small diameter, and the

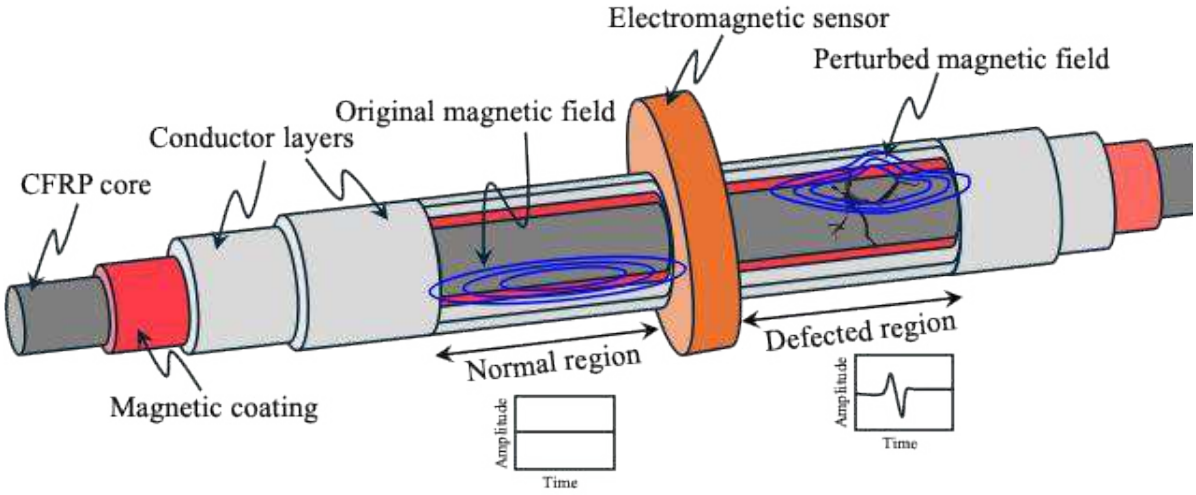
compressive stress exceeds the ultimate compressive strength. Therefore, defect monitoring of the composite core in ACCC wires during manufacturing or after tower installation is necessary to address safety problems.

Some methods can be used to inspect power transmission lines without damaging conductors. The most widely used method is the use of thermal or visual images captured using an infrared (IR) camera or high-definition vision sensors. Many images are collected to detect insulator defects or damage to infrastructure (Z. Liu et al., 2022). In addition, when a component is damaged or a defect is generated at the surface of a transmission line, local heating occurs, enabling IR cameras to easily detect anomalies. These cameras or sensors can be mounted on drones or unmanned aerial vehicles (UAVs) to cover a wide inspection area in a short period (Jeong et al., 2023; Xu et al., 2022). Because of the height of the transmission line towers, UAVs are convenient and have no obstacles at that altitude. Currently, UAVs can be driven without manual control and guided by a convolutional neural network (CNN) algorithm that can extract power lines from images (Li et al., 2023; Xu et al., 2022).

However, image-based inspection methods can only detect anomalies on the surfaces of transmission lines. Cracks generated in the composite core of ACCC wires are internal defects that are covered by multiple aluminum conductor layers, making conventional imaging methods impractical. X-ray systems can be an alternative method for inspecting hidden defects from a surface (Wang et al., 2023). The X-ray energy density is attenuated by the material thickness and density. When defects or voids are present, more energy decreases because of the change in properties compared with normal locations. Energy can be mapped onto images that provide the user with better visualization and artificial intelligence algorithms can be incorporated (Hu et al., 2021, 2024). Although the X-ray method has good detection ability and provides high-resolution images of internal cracks in ACCCs, several challenges must be considered. The X-ray method requires high power to generate photon energy that can penetrate through the aluminum layers, which makes the equipment bulky. X-ray tubes generate heat that requires air or liquid cooling to ensure system reliability. Additionally, some safety issues are associated with X-ray radiation for operators; therefore, proper shielding of equipment is a critical factor. Considering these

concerns, the cost of the system is high, which prevents industrial users from applying the method in the field.

Eddy current testing (ECT) is a widely used method in the field of nondestructive testing (NDT) that inspects defects by generating eddy currents in electrically conductive materials (Mazzeschi et al., 2023; Sun et al., 2021; Trung et al., 2024). The ECT system is simple and relatively inexpensive compared with other NDT methods, such as the X-ray method. The sensor consists of two coils, each used for electromagnetic field generation and reception. When a defect is present, the eddy current density changes, perturbing the net magnetic flux density. The ECT method is highly sensitive for crack detection. Most studies on ECT applications in transmission lines have focused on the detection of defects in aluminum conductors (Liao et al., 2022; Xia et al., 2013). Researchers utilized pulsed eddy currents to overcome the limitations of skin depth associated with the application of a single frequency in the coil. Pulse signals comprise multiple frequency components that enable the detection of changes at varying depths through analysis of each component. The sensor can be mounted on an inspection robot to remotely identify defects in transmission lines. Defects can be identified by studying the received signals, specifically variations in the amplitude of peak signals or the slope during pulsed eddy current application, and by assessing the voltage differential using single-frequency approaches. However, difficulties remain when utilizing the existing ECT method for ACCCs, which commonly have defects in the internal composite cores. As mentioned previously, the ACCC comprises two twisted layers of aluminum conductors with a carbon-fiber composite core. The entire structure of the actual ACCC used in overhead transmission lines is shown in Fig. 1. Detecting changes in the core structure from the outside of the conductor using the conventional ECT method is very challenging owing to the weak electromagnetic properties of the CFRP. Moreover, the aluminum strands act as a shield around the core, preventing the generation of eddy currents in the carbon fibers by high-frequency electromagnetic fields. The ACCC must be inspected for defects before installation and periodically monitored during operation. However, owing to the aforementioned problems, several challenges exist. Therefore, a proper NDT method is required for detecting ACCC defects.



(a)

Fig. 1. Structure and inspection period of ACCC

This paper presents a defect inspection system for composite cores in ACCC wires that utilizes an electromagnetic sensor and magnetic coating interlayer to improve the magnetic characteristics of the composite surface. In this study, we employed a method that detects distortions in the electromagnetic field generated from the outer surface of the ACCC and penetrates inward, with such distortions indicating the presence of defects in the composite core. However, under typical conditions, the electromagnetic field passing through conductors 1 and 2 is too weak to effectively assess the state of the core. To address this, we propose a magnetic coating layer on the core to increase its magnetic permeability, thereby enhancing the detection of defects within the core. When a brittle defect occurs in the composite core with a magnetic coating, the coating in the defect region is damaged, affecting the impedance of the electromagnetic sensor-based monitoring system as shown in Fig. 1. Hence, this study analyzed the correlation between electromagnetic field and magnetic coatings based on continuum mechanics-based theory and designed a monitoring system accordingly. The boundary conditions of the electric field and the intensity of the magnetic field were determined in the event of variations in the magnetic permeability of the coating material. The increase in electrical dissipation

was attributed to a decrease in permeability. An electromagnetic sensor was designed to detect defects in the composite core with high sensitivity. To enhance monitoring performance, this study developed a magnetic coating by mixing epoxy resin with magnetic particles. Increasing the proportion of magnetic particles improves the permeability; however, it also reduces the adhesion to the composite core, resulting in decreased reliability. Therefore, an optimized magnetic coating design is required. Subsequently, a magnetic coating was fabricated by optimizing the thickness and volumetric magnetic particle density to optimize the adhesion and sensor signal-to-noise ratio (SNR) using finite element method (FEM) data. Finally, the experiments confirmed the efficacy of the electromagnetic field inspection and magnetic coating approach, illustrating the superior detectability of internal faults in the ACCC.

The remainder of this paper is organized as follows. Section 2 presents a theoretical analysis of the conductor–coating interface boundary conditions derived from Maxwell's equations in the presence of coating defects for the system design. Sections 3 and 4 detail the design of the electromagnetic sensors and the coating material, respectively. Section 5 confirms the monitoring methodology, and Section 6 concludes the paper.

2. Theoretical discussion for the system design

Electromagnetic fields can be explained by Maxwell's equations as follows (Kim et al., 2025; Y. Liu et al., 2022).

$$\nabla \cdot \mathbf{d} = \rho_e, \tag{1a}$$

$$\nabla \cdot \mathbf{b} = 0, \tag{1b}$$

$$\nabla \times \mathbf{e} = -\mu \frac{\partial \mathbf{h}}{\partial t}, \tag{1c}$$

$$\nabla \times \mathbf{h} = \mathbf{j} + \frac{\partial \mathbf{d}}{\partial t}. \tag{1d}$$

In the aforementioned equations, **b** denotes the magnetic flux density, and **h** specifies the magnetic-field intensity. **e** represents the electric field, and **d** indicates the electrical displacement. The current

density is represented as **j**. Equations (1a) and (1b) express Gauss's flux theorem and the law of magnetism, respectively. Equation (1a) shows that the flux flowing from the surface is proportional to the electric charge, whereas Eq. (1b) indicates the absence of monopoles in the electric charge. Equations (1c) and (1d) represent Faraday's law and the Ampere–Maxwell law, respectively. Each equation shows the relationship between the electric and magnetic fields. ρ_e is the charge density, and μ denotes for the magnetic permeability. In this model, we assume that the observer and measurement subject are fixed in the same space–time frame without relative velocity, and the effects of relativity are neglected, as in other engineering applications (Lee, 2021, 2024; Shim et al., 2025; Sim et al., 2024).

Each specific term in Maxwell's equations can be defined through electromagnetic constitutive equations and Ohm's law as

$$\mathbf{b} = \mu\mathbf{h}, \tag{2a}$$

$$\mathbf{d} = \varepsilon\mathbf{e}, \tag{2b}$$

$$\mathbf{j} = \sigma\mathbf{e}, \tag{2c}$$

where ε and σ denote the electrical permittivity and conductivity, respectively. Electromagnetic properties vary depending on the material and can be measured experimentally.

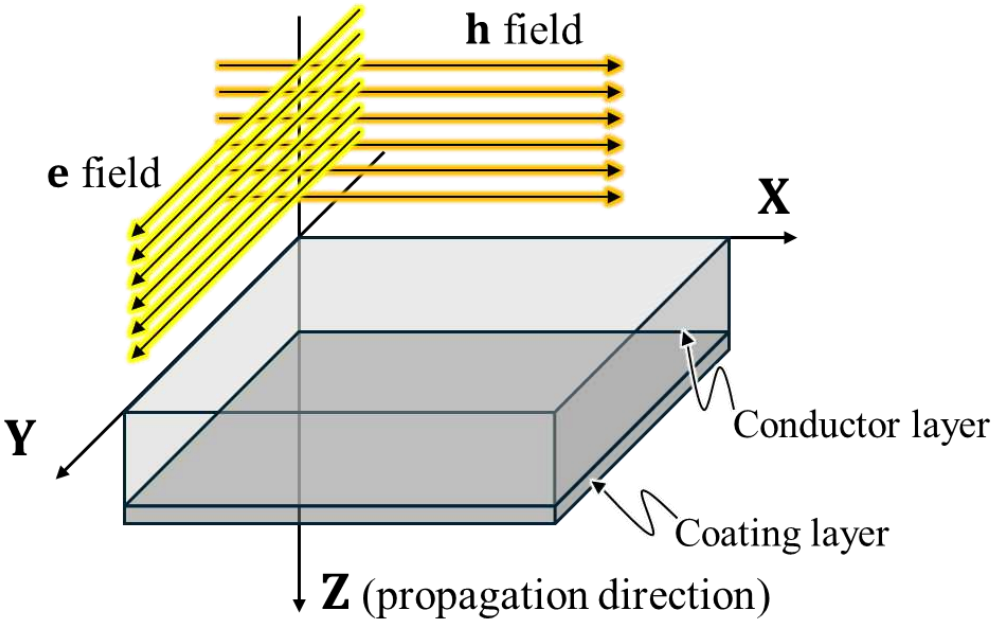


Fig. 2. Schematic of the plane wave approximation of electromagnetic fields

When utilizing an electromagnetic sensor for ACCC inspection, the driving frequency range is extremely low because of skin depth, resulting in a significant wavelength of the generated electromagnetic waves. Consequently, electromagnetic waves can be approximated as plane waves characterized by a uniform amplitude and phase throughout the propagation path, as shown in Fig. 2. Calculating the curl of Eq. (1d) and substituting the curl of the electric field into Eqs. (1c) with (2) results in

$$\nabla \times \nabla \times \mathbf{h} = \nabla \times \sigma\mathbf{e} + \nabla \times \varepsilon \frac{\partial \mathbf{e}}{\partial t}, \tag{3a}$$

$$\nabla \times \nabla \times \mathbf{h} = \nabla(\nabla \cdot \mathbf{h}) - \nabla^2 \mathbf{h}\,, \tag{3b}$$

$$-\nabla^2 \mathbf{h} = -\sigma\mu \frac{\partial \mathbf{h}}{\partial t} - \varepsilon\mu \frac{\partial^2 \mathbf{h}}{\partial t^2}\,. \tag{3c}$$

Assuming the $\mathbf{h}$ field is in a sinusoidal form $\mathbf{h} = \mathbf{h}_0 e^{j\omega t}$, then the time derivatives in Eq. (3c) can be expressed as

$$\nabla^2 \mathbf{h} = j(\sigma\mu\omega + j\varepsilon\mu\omega^2)\mathbf{h}, \tag{4a}$$

$$\nabla^2 \mathbf{h} = k^2 \mathbf{h}, \tag{4b}$$

where

$$k = \sqrt{j\mu\omega(\sigma + j\varepsilon\omega)}\,. \tag{4c}$$

ω is the operating frequency, and j is the complex number component. The $\mathbf{h}$ field has a gradient in the z-direction, where its components change, and it has a constant component in the x-direction; $\frac{\partial \mathbf{h}}{\partial x} = \frac{\partial \mathbf{h}}{\partial y} = 0$. Subsequently, Eq. (4b) can be rewritten as the total derivative in the z-direction. The solution of the differential equation is

$$\begin{aligned} &\mathbf{h} = h_x \bar{\mathbf{e}}_x \text{ where,} \\ &h_x = h_0 e^{-kz}. \end{aligned} \tag{5}$$

$\bar{\mathbf{e}}_x$ is the x-direction base vector of the Cartesian coordinate. k denotes the propagation constant that controls the absorption and phase changes in the magnetic field. The amplitude decay is caused by the generated induced current and secondary magnetic field, according to Lenz's law. The propagation

constant is defined differently for conductive and dielectric materials (Park et al., 2025). The electrical conductivity σ is very large compared with $\varepsilon\omega$ for conductors such as aluminum and copper. Therefore, the propagation constant and h_x for the conductor and dielectric can be defined differently as

$$h_{\mathrm{c,x}} = h_0 \exp\left(-\sqrt{\frac{\mu_{\mathrm{c}}\sigma\omega}{2}}z\right)\exp\left(-j\sqrt{\frac{\mu_{\mathrm{c}}\sigma\omega}{2}}z\right), \text{where } k_{\mathrm{c}} = (1+j)\sqrt{\frac{\mu_{\mathrm{c}}\sigma\omega}{2}} \text{ for the conductor,} \tag{6a}$$

$$h_{\mathrm{d,x}} = h_0 \exp\left(-j\omega\sqrt{\mu_{\mathrm{d}}\varepsilon}z\right), \text{where } k_d = j\omega\sqrt{\mu_{\mathrm{d}}\varepsilon} \text{ for the dielectric.} \tag{6b}$$

where k_{c} is the propagation constant of the conductor, and k_{d} is the propagation constant of the dielectric material (magnetic coating). $h_{\mathrm{c},x}$ and $h_{\mathrm{d},x}$ denote the **h** fields in the x-direction for the conductor and dielectric, respectively. Subscripts c and d in μ represent the magnetic permeability for conductor and dielectric. The first exponential term in $h_{\mathrm{c,x}}$ represents the decay of the magnetic field according to the induced current, and the second term explains the phase change in the z-direction. This indicates that the amplitude and phase change simultaneously for the conductors. However, only the phase change term is included for the dielectric material according to the near-zero conductivity, as shown in Eq. (6b). With Eqs. (1c), (6a), and (6b), the electric field in the y-direction can be defined as

$$\mathbf{e}_{\mathrm{c}} = e_{\mathrm{c},y}\bar{\mathbf{e}}_y, \text{ where } e_{\mathrm{c},y} = j\omega\mu_{\mathrm{c}}\frac{h_{\mathrm{c,x}}}{k_{\mathrm{c}}}, \tag{7a}$$

$$\mathbf{e}_{\mathrm{d}} = e_{\mathrm{d},y}\bar{\mathbf{e}}_y, e_{\mathrm{d},y} = j\omega\mu_d\frac{h_{\mathrm{d,x}}}{k_{\mathrm{d}}}. \tag{7b}$$

$\bar{\mathbf{e}}_y$ is the y-direction base vector of the Cartesian coordinate. Owing to the uniform magnetic-field intensity in the x-direction, the electric field has only one component in the y-direction. A magnetic coating is used to monitor changes in the composite core of the ACCC. When a crack is generated in the core, the coating departs locally from the CFRP and loses its magnetic permeability. A change in magnetic properties simultaneously perturbs the electric field and magnetic intensity. However, even in a defect scenario, the **e** and **h** fields must satisfy the electromagnetic boundary conditions between the conductor and dielectric. The tangential magnetic intensity and electric field density must be equal under the boundary conditions:

$$\mathbf{h}_{\mathrm{c}}^{\parallel} + \Delta\mathbf{h}_{\mathrm{c}}^{\parallel} = \mathbf{h}_{\mathrm{d}}^{\parallel} + \Delta\mathbf{h}_{\mathrm{d}}^{\parallel}, \tag{8a}$$

$$\mathbf{e}_{\mathrm{c}}^{\parallel} + \Delta\mathbf{e}_{\mathrm{c}}^{\parallel} = \mathbf{e}_{\mathrm{d}}^{\parallel} + \Delta\mathbf{e}_{\mathrm{d}}^{\parallel}. \tag{8b}$$

In the above equation, the superscript ∥ represents the tangential direction of the magnetic intensity and the electric field. $\Delta\mathbf{h}^{\parallel}$ and $\Delta\mathbf{e}^{\parallel}$ are the changes in magnetic intensity and electric field, respectively, caused by a magnetic permeability change in the dielectric part. The boundary condition of the magnetic-field intensity can be satisfied using Eq. (7) as follows.

$$\frac{k_{\mathrm{c}}(e_{\mathrm{c,y}}+\Delta e_{\mathrm{c,y}})}{j\omega\mu_{\mathrm{c}}} = \frac{k'_{\mathrm{d}}(e_{\mathrm{d,y}}+\Delta e_{\mathrm{d,y}})}{j\omega\mu'_{\mathrm{d}}}. \tag{9}$$

Only the component in the y-direction is considered according to the plane-wave approximation. μ'_{d} is the change in the magnetic permeability of the coating material caused by defect induced detachment. The propagation constant also changes with the material property dependency. The perturbed propagation constant can be expressed as

$$k'_{\mathrm{d}} = j\omega\sqrt{(\mu_{\mathrm{d}} - \Delta\mu)\varepsilon} \approx j\omega\sqrt{\mu_{\mathrm{d}}\left(1 - \frac{\Delta\mu}{\mu_{\mathrm{d}}}\right)\varepsilon} \approx k_{\mathrm{d}}\left(1 - \frac{\Delta\mu}{2\mu_{\mathrm{d}}}\right), \tag{10a}$$

$$\frac{1}{\mu_{\mathrm{d}}'} \approx \frac{1}{\mu_{\mathrm{d}} - \Delta\mu} \approx \frac{1}{\mu_{\mathrm{d}}\left(1 - \frac{\Delta\mu}{\mu_{\mathrm{d}}}\right)} \approx \frac{1}{\mu_{\mathrm{d}}}\left(1 + \frac{\Delta\mu}{\mu_{\mathrm{d}}}\right). \tag{10b}$$

The perturbed propagation constant and reciprocal of the dielectric magnetic permeability can be approximated using a Taylor series expansion. Substituting the perturbed values in Eq. (9) with Eq. (10) yields

$$\frac{k_{\mathrm{c}}}{\mu_{\mathrm{c}}}\left(e_{\mathrm{c,y}} + \Delta e_{\mathrm{c,y}}\right) = \frac{k_{\mathrm{d}}}{\mu_{\mathrm{d}}}\left(1 - \frac{\Delta\mu}{2\mu_{\mathrm{d}}}\right)\left(1 + \frac{\Delta\mu}{\mu_{\mathrm{d}}}\right)(e_{\mathrm{d,y}} + \Delta e_{\mathrm{d,y}}). \tag{11}$$

From the electric-field boundary condition shown in Eq. (8b), electric fields $e_{\mathrm{c,y}}$ and $e_{\mathrm{d,y}}$ are identical. Additionally, $\Delta e_{\mathrm{c,y}}$ and $\Delta e_{\mathrm{d,y}}$ are equal; thus, we can rearrange Eq. (11) in terms of $e_{\mathrm{c,y}}$ as follows:

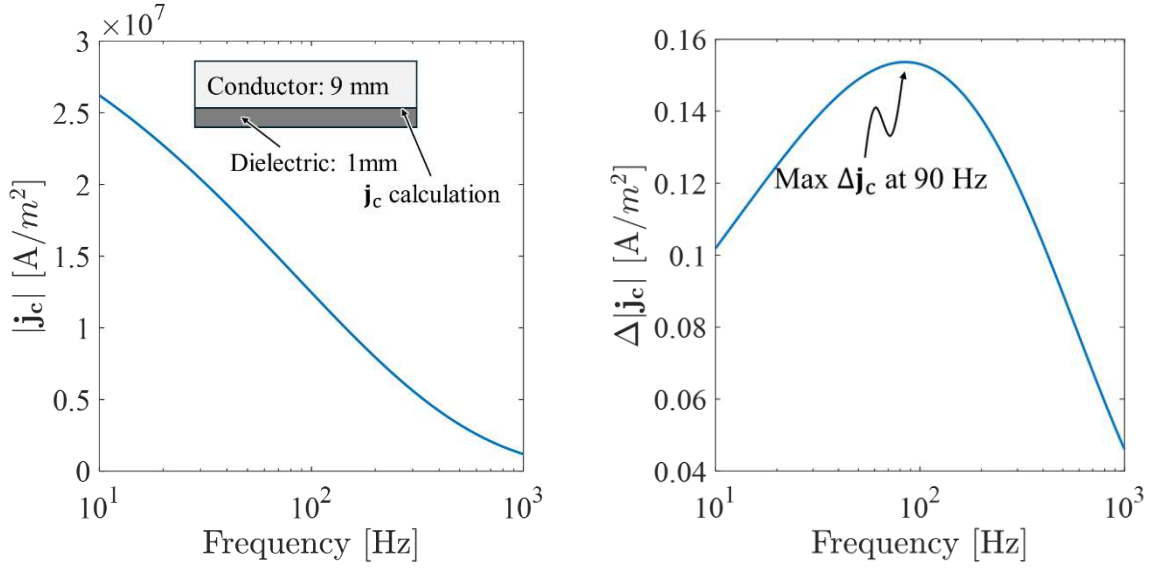
$$\Delta j_{\mathrm{c,y}} = \sigma\left(\frac{2\mu_{\mathrm{c}}\mu_{\mathrm{d}}k_{\mathrm{d}} - 2\mu_{\mathrm{d}}^2 k_{\mathrm{c}} + \mu_{\mathrm{c}}k_{\mathrm{d}}\Delta\mu}{2\mu_{\mathrm{d}}^2 k_{\mathrm{d}} - 2\mu_{\mathrm{c}}\mu_{\mathrm{d}}k_2 - \Delta\mu}\right)e_{\mathrm{c,y}}. \tag{12}$$

In the above equation, the change in the current density in the conductor at the boundary depends on the change in the magnetic permeability of the coating and the initial electric field (before the defect) on the conductor side at the boundary. This shows that defects affect the amount of electrical dissipation

in the conductor. This change is reflected in the received signals and impedance of the pickup coil in the electromagnetic sensor. The defects are captured by detecting changes in impedance.

Based on the discussed equations, the variation in current density resulting from the alteration in the magnetic permeability of the coating is calculated. The structure consists of a 9 mm thick conductor with a 1 mm dielectric placed below. The electrical conductivity of the conductor is defined at 37 MS/m, and the relative magnetic permeability of the dielectric layer is 1.3. These specifications are consistent with the simulation and experimental values addressed later. The frequency range for the calculation is 10–1000 Hz. The calculated results for the initial and altered current densities with respect to the defects are shown in Fig. 3. The current density was computed for the conductor region at the boundary at a depth of 9 mm.

The normal case with no defects in the coating is depicted in Fig. 3a, where $\Delta\mu$ equals zero, resulting in the absolute values of current density. The current density decreases with respect to frequency. This phenomenon is caused by the skin effect, wherein most of the current density is concentrated at the surface and absorbed before reaching the bottom surface of the conductor. However, when a flaw occurs in the coating, resulting in a reduction in the magnetic permeability, the variation in the current density exhibits a distinct trend. The current density exhibits an upward tendency in the lower frequency range, peaking at approximately 90 Hz. The trend reverses and reaches a minimal value at 1000 Hz. This is primarily caused by the skin depth of the current induced by the electromagnetic field. According to Eqs. (6) and (7a), the electric field within the conductor is enhanced by the magnetic field intensity, which is affected by the frequency. Nevertheless, the skin depth decreases with increasing frequency, inhibiting the electric field energy from penetrating the surface of the conductor. This calculation confirms that the impact of the defect on the current density is strongest at 90 Hz. Consequently, an electromagnetic sensor capable of generating electromagnetic fields at approximately 90 Hz should be developed.



(a) (b)

Fig. 3. Change in current density by frequency: (a) Current density with no defect in coating and (b) current density change in coating permeability loss

3. Design of the electromagnetic sensors

As noted in Section 2, the electromagnetic sensor is operated at approximately 90 Hz for clear visible flaw detection. An electromagnetic sensor typically comprises a drive coil and pickup coil. Drive coils utilize thicker wires than pickup coils to reduce the resistance and enhance the magnetic-field strength. Conversely, pickup coils have a greater number of turns to enhance the sensitivity of detecting variations in the net magnetic field. The design specifications of the electromagnetic sensor include the number of turns, wire diameter, inner coil diameter, and coil height. The computation of the inductance is a crucial aspect of sensor design. Magnetic fields must be produced effectively at a specified frequency. The Wheeler formula is employed to calculate the inductance of the multilayer solenoid, which serves as an empirical model based on the geometrical specifications of the sensor. The equation used is as follows: (Wheeler, 1942)

$$\mathrm{L[\mu H]} = \frac{0.8N^2r^2}{6r+9l+10c}. \tag{13}$$

where N represents the number of turns in the sensor, and r signifies the average radius of the entire

coil from the centerline. l denotes the length of the sensor, and c represents the distance from the inner radius to the outer radius. Table 1 lists the results for the specified sensor parameters. The total impedance and phase values were determined from the computed inductance. The impedance values were computed over the frequency range of 1–500 Hz. The impedance and phase of the electromagnetic sensor are shown in Fig. 4. The impedance values increase approximately linearly with frequency for both coils. In the low working frequency range, the parasitic capacitance, which is the primary contributor to the inductor resonance, is negligible. The phase increases and reaches saturation beyond 100 Hz for the drive coil. The phase angle at 100 Hz is 1.15 rad, indicating that the inductive component of the impedance exceeds the resistive component by a factor of more than 2.2. We can conclude that the drive coil is functional at this point.

Table 1. Electromagnetic sensor parameter specifications

Sensor	Parameter	Value	Units
Drive coil	Inner radius	18.0	[mm]
	Width	15.0	
	Length	25.0	
	Wire diameter	0.44	
	Number of turns	1937	[-]
Pickup coil	Inner radius	18.0	[mm]
	Width	13.0	
	Length	8.0	
	Wire diameter	0.18	
	Number of turns	2336	[-]

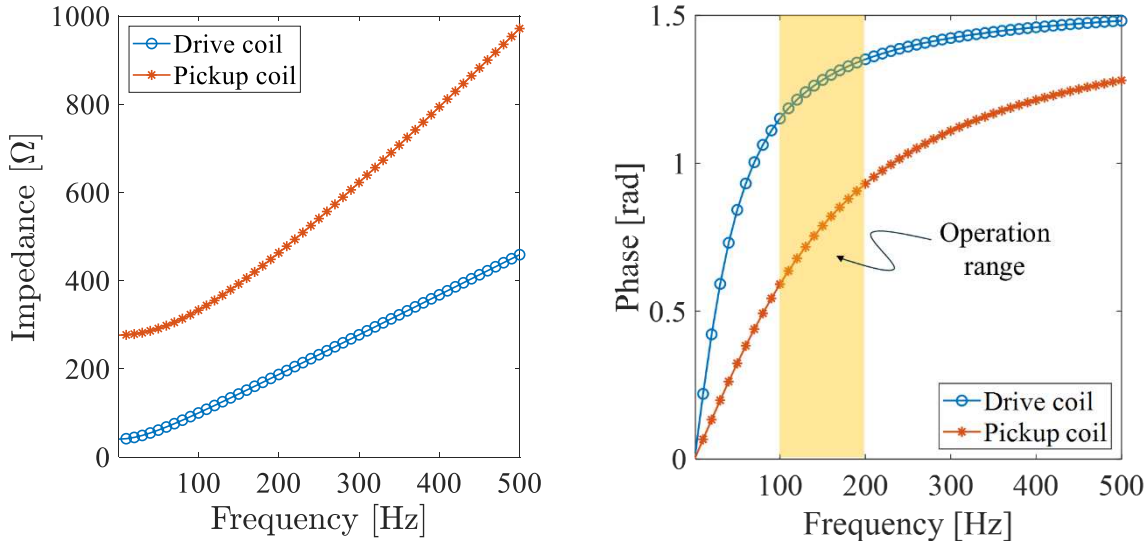
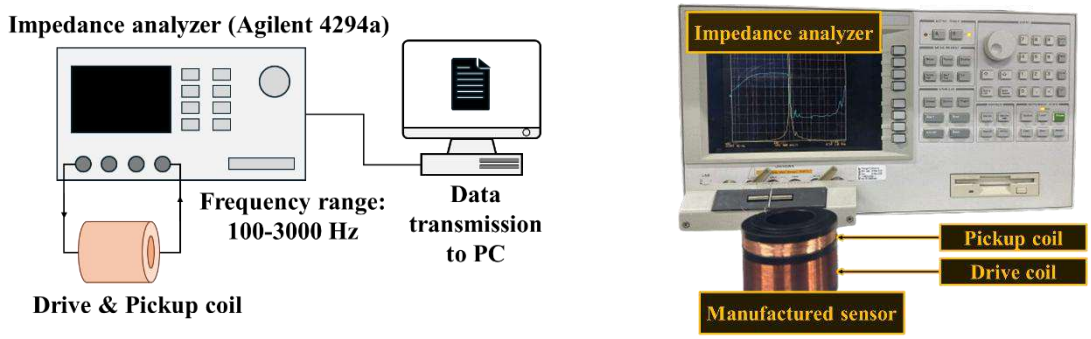


Fig. 4. Calculated electrical properties of designed coil: (a) Impedance and (b) phase angle results

256

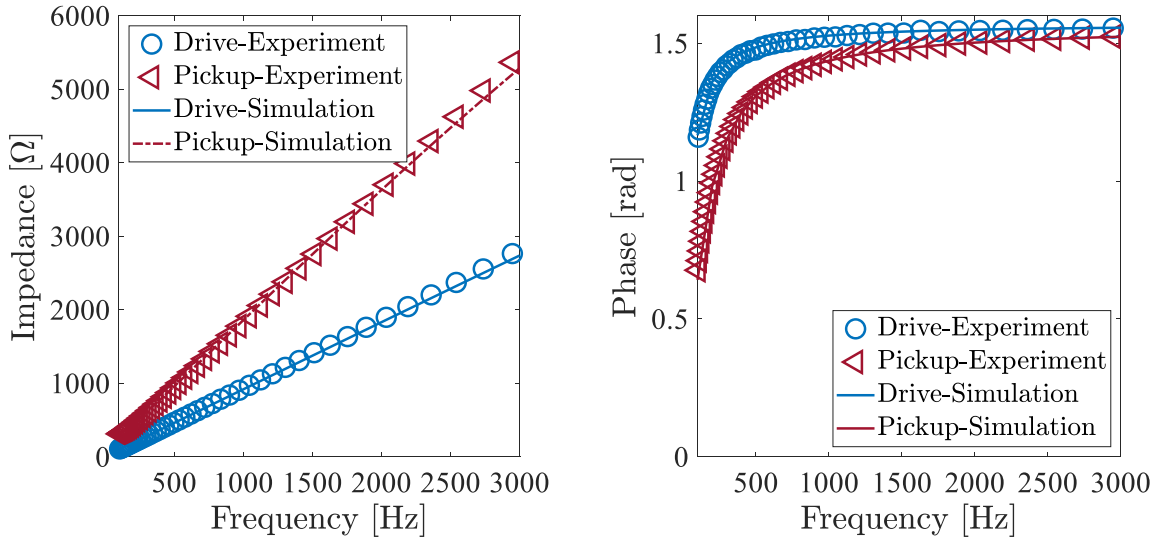
257 The electromagnetic sensor was manufactured using the parameters listed in Table 1. The
258 performance of the electromagnetic sensor was verified by evaluating the impedance and phase
259 characteristics of the drive and pickup coils through experiments and simulations. The experimental
260 measurements were performed using an impedance analyzer (Agilent 4294A) with the manufactured
261 coils. The electrical characteristics were analyzed by changing the excitation frequency applied to the
262 coils from 100 to 3000 Hz. Figure 5 shows the detailed schematic and experimental setup. In addition
263 to the experiments, electromagnetic simulations were conducted to numerically validate the results. The
264 simulations were conducted using COMSOL Multiphysics software. Frequency-domain analysis was
265 performed with the AC/DC module, including the identical frequency range of 100–3000 Hz employed
266 in the experimental studies. The coil parameters used in the simulation were obtained from the design
267 values listed in Table 1. The validation results are presented in Figure 6. The simulation results, as
268 depicted in the figure, closely agreed with the experimental tendencies, exhibiting minimum errors. The
269 phase responses of each coil demonstrated a strong correlation between the simulated and experimental
270 data, similar to the impedance data. The phase of the drive coil at 100 Hz was measured as 1.16 rad,
271 closely corresponding with the originally planned value. The results confirmed that the electrical

properties of the fabricated coils agreed with the design parameters obtained using both experimental and numerical methods.



(a) (b)

Fig. 5. Experimental setup of impedance test; (a) schematic view of the test setup and (b) actual setup of the manufactured coils



(a) (b)

Fig. 6. Experimental and numerical results of impedance analysis: (a) impedance results and (b) phase results

4. Development of the magnetic coating interlayer

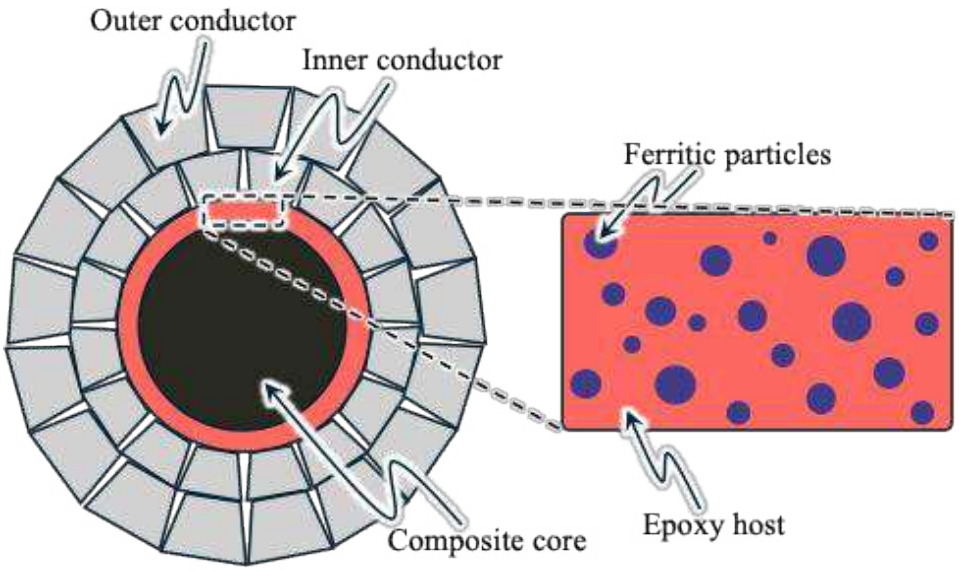


Fig. 7. Schematic of the cross-section view of the magnetic coating applied to the composite core

277

278 A magnetic coating was deposited on the surface of the core to monitor the defects in the composite
279 core by altering the magnetic properties of the core surface. The magnetic coating influences the
280 magnetic flux when a crack occurs in the composite core. As mentioned in Section 2, the removal of
281 the magnetic coating resulting from the defect influences the current induced at the conductor–coating
282 interface. The coating was fabricated by combining ferritic steel particles with an epoxy host, as shown
283 in Fig. 7. Enhancing the relative magnetic permeability by increasing the volumetric or mass ratio can
284 improve the detection capabilities of electromagnetic sensors. Equation (12) indicates that the
285 magnitude of the permeability alteration and the disparity in the properties of the coating and air directly
286 influence the induced current. However, excessive increases are not feasible because they weaken the
287 adhesive strength between the coating and the composite core. Consequently, simulations are essential
288 for analyzing the influence of the thickness of the coating material and the magnetic permeability on
289 the signal responses to artificial flaws. Initially, the equations employed to calculate the relative
290 magnetic permeability must be formulated to perform accurate simulations.

291 The effective magnetic permeability of a mixture of materials containing magnetic particles in a host
292 matrix must be determined. The effective permeability can be utilized in FEM simulations to analyze

the responses of the developed electromagnetic sensor to defects in the magnetic coating. These results can be utilized to optimize the thickness and particle volumetric ratio of coatings. The axisymmetric magnetic scalar potential within a particle can be expressed using Laplace's general equation (Sihvola, 1999):

$$\psi_{\text{in}}(r,\theta) = -ar\cos(\theta), \tag{14a}$$

$$\psi_{\text{out}}(r,\theta) = -h_0 r\cos(\theta) + \frac{b\cos(\theta)}{r^2}, \tag{14b}$$

where

$$h_0 = |\mathbf{h}_0|. \tag{14c}$$

In this equation, ψ_{in} is the magnetic scalar potential in the magnetic sphere, and ψ_{out} represents the magnetic scalar potential outside the sphere. h_0 is the absolute value of the magnetic-field intensity vector $\mathbf{h}_0$. a and b are model parameters of the magnetic scalar potential. r denotes the radius from the center of the sphere. The subscripts “in” and “out” represent the internal domain of the sphere and the outside domain, respectively. These expressions are written in spherical coordinates, according to the axial symmetry of the geometry. The addition term in Eq. (14b), which is proportional to $1/r^2$, is the effect of the induced magnetic dipole. The scalar potential and magnetic field must satisfy the following boundary conditions:

$$\psi_{\text{in}} = \psi_{\text{out}}, \tag{15a}$$

$$\mathbf{b}_{\text{in}}^{\perp} = \mathbf{b}_{\text{out}}^{\perp}. \tag{15b}$$

From Eqs. (14) and (15a), the model parameter b can be rearranged as $aR^3 - h_0R^3$ when $r = R$. The perpendicular parts of the magnetic flux density at the surface are calculated as follows:

$$h_r = -\frac{\partial\psi}{\partial r}, \tag{16a}$$

$$h_{\text{in}} = a\cos(\theta), \tag{16b}$$

$$h_{\text{out}} = h_0\cos(\theta) + \frac{2b\cos(\theta)}{r^3}, \tag{16c}$$

$$a = \frac{3\mu_h}{\mu_p + 2\mu_h} h_0, \tag{16d}$$

where h_r is the magnetic-field intensity in the r component direction. From the magnetic-field intensities inside and outside the spherical domain, as shown in Eqs. (16b) and (16c), the boundary conditions in Eq. (15b) can be solved. Utilizing the rearranged b, model parameter a can be derived using Eq. (16d). μ_p and μ_h are the magnetic permeabilities of the particle and host material, respectively. As mentioned previously, the $1/r^2$ term in Eq. (14b), is caused by the magnetic dipole effect. The general form of the dipole potential at large distances is (Jackson, 1998)

$$\psi_{dip} = \frac{m\cos(\theta)}{4\pi r^2}. \tag{17}$$

where m is the magnetic dipole moment. Therefore, using Eqs. (14b) and (17), the model parameter b can be defined as

$$b = \frac{m}{4\pi}. \tag{18}$$

From the rearrangement of b and the definition of the model parameter a shown in Eq. (16d), the model parameter b is defined as

$$b = R^3 \left(\frac{\mu_\mathrm{p}-\mu_\mathrm{h}}{\mu_\mathrm{p}+2\mu_\mathrm{h}}\right) h_0, \tag{19}$$

The induced magnetic dipole moment is related to the external magnetic-field intensity. Combining Eqs. (18) and (19), the magnetic dipole moment of the particle is defined as

$$m = \alpha_m h_0, \tag{20a}$$

$$\alpha_m = 3V \frac{\mu_\mathrm{p}-\mu_\mathrm{h}}{\mu_\mathrm{p}+2\mu_\mathrm{h}}. \tag{20b}$$

where V is the volume of the sphere. In the above equation, α_m is the magnetic polarizability of the particles. The effective magnetization of the dipoles in the host medium can be expressed as

$$M_\mathrm{eff} = N\alpha_m h_\mathrm{local}, \tag{21a}$$

$$M_\mathrm{eff} = \left(\frac{\mu_\mathrm{eff}-\mu_\mathrm{h}}{\mu_\mathrm{h}}\right) h_0, \tag{21b}$$

$$\frac{\mu_\mathrm{eff}-\mu_\mathrm{h}}{\mu_\mathrm{eff}+2\mu_\mathrm{h}} = f\frac{\mu_\mathrm{p}-\mu_\mathrm{h}}{\mu_\mathrm{p}+2\mu_\mathrm{h}}, \tag{21c}$$

where

$$\mu_{\text{eff}} = \mu_{\text{h}}(1 + \chi_{\text{eff}}). \tag{21d}$$

$$h_{\text{local}} = h_0 + \frac{M}{3}. \tag{21e}$$

N represents the particle count within a unit volume, and f denotes the volumetric fraction of these particles relative to the total volume of the coating, denoted as $N \cdot V$. The effective magnetization of the coating material is determined by the density of the magnetic dipoles per unit volume. The magnetization is determined using the susceptibility of the effective media, as shown in Eq. (21d), illustrating the effective magnetic permeability of the coating. The supplementary field $M/3$ is the self-field generated by a dipole. Assuming Eqs. (21a) and (21b) are equivalent, and rearranging the terms yields the relationship between the effective magnetic permeabilities of the coating, particle, and host material with respect to the volume fraction of the particles, as expressed in Eq. (21e). The effective magnetic permeability of the coating is defined as

$$\mu_{\text{eff}} = \mu_{\text{h}} \left[1 + 3f \frac{\mu_{\text{p}} - \mu_{\text{h}}}{2\mu_{\text{h}} + \mu_{\text{p}} - f(\mu_{\text{p}} - \mu_{\text{h}})}\right]. \tag{22}$$

This equation is known as the Maxwell–Garnett equation (Chang & Liao, 2011) and determines the effective magnetic permeability of a medium containing particles within the host material. This equation was applied to estimate magnetic permeability and validated via numerical simulations.

The magnetic coating is employed to detect the defects occurring within the composite cores of the ACCC. The coating fails concurrently with the composite when the bending stress exceeds the fracture threshold. To develop a magnetic coating for electromagnetic-sensor-based monitoring, we combined spherical ferrite steel particles with an epoxy polymer and cured using an infrared heater. The particle size limit was set to 5 μm.

The probability of detection increases with increasing magnetic permeability and coating thickness. The coating should be combined with larger particle densities to enhance the magnetic permeability; however, this compromises the adhesion between the coating and the composite core surface. Consequently, the volumetric fraction of the particles and the thickness must be adjusted with respect to the response of the electromagnetic sensor to the defect and the removal rate. The magnetic coating

prototype was created with particle mass densities of 20, 40, and 60 wt% and applied to glass substrates with thicknesses of 25, 50, 75, and 100 μm. The adjustment of the coating particle density and thickness was validated using ECT simulations using the FEM software and analyzing the variations in the sensor impedance. The adhesion test for each coating was conducted according to the ASTM-D3359 standard, which involved cutting the coating into 25 square sections with a sharp razor and removing the material from the substrate with tape.

The effective permeabilities of the prototype coatings were initially computed using the Maxwell–Garnett formula, as presented in Eq. (22). The formula, predicted on the volumetric ratio, facilitated the conversion of the weight percent density by utilizing the densities of the epoxy and ferritic steel particles. The density of the epoxy polymer was set to 1280 kg/m^3, whereas that of the ferritic steel was fixed at 7830 kg/m^3. The volumetric ratios for 20, 40, and 60 wt% densities were calculated to be 0.0393, 0.0983, and 0.197, respectively. Polymers are not magnetic materials because their magnetic permeability is 1. The magnetic permeability of ferritic steel particles was assumed to be 100. Substituting the volumetric ratios and magnetic permeabilities of each material into Eq. (22), the effective magnetic permeability of the prototype coating was determined. The calculated effective magnetic permeabilities were 1.12, 1.32, and 1.71 for volumetric ratios of 0.0393, 0.0983, and 0.197, respectively. The permeability data are presented in Table 1.

Table 1 Magnetic permeability of the prototype specimens

f [-]	Maxwell–Garnett μ_r[-]	Thickness [μm]
0.0393	1.12	25
		50
		75
		100
0.0983	1.32	25
		50
		75

		100
0.197	1.71	25
		50
		75
		100

Simultaneous experiments and numerical simulations were performed to validate the calculated Maxwell–Garnett effective magnetic permeability (Table 1). The experimental setup involved positioning a coil on the surface of the coating and measuring the change in the inductance ratio relative to the initial value using an LCR meter. The inductance increased corresponding to the magnetic dipoles in the coating, which concentrated the magnetic-field lines and strengthen the magnetic flux linkage. The experimental coil had an inductance of 20 mH and the excitation frequency was fixed at 10 kHz on the coated surface. The experimental configuration is shown in Fig. 5. Experiments were conducted on 12 specimens, as listed in Table 1.

Numerical simulations were performed by modeling a coil equivalent to that used in the tests using COMSOL Multiphysics. Parametric studies were performed during the simulations by varying the relative magnetic permeability of the material from 1 to 2 in increments of 0.02. The thickness ranged from 25 to 100 μm in 25 μm increments. The simulation results indicated that the inductance ratio function, κ, was determined by correlating it with the relative magnetic permeability. This was compared with experimental measurements to inversely predict the true permeability of the material. Figure 8 shows the experimental setup and coil geometry used in the simulation.

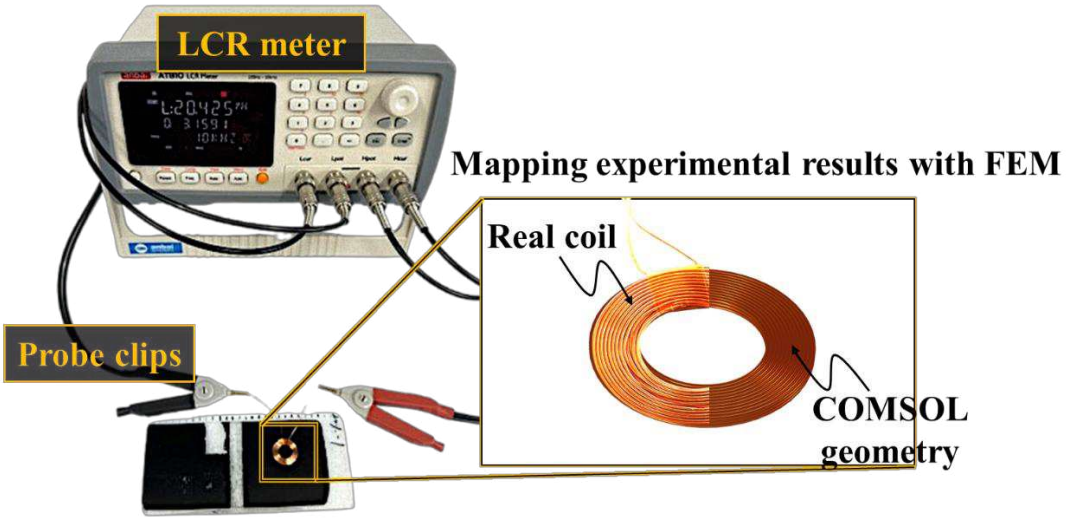


Fig. 8. Experimental setup for magnetic permeability determination

Figure 9 shows the results of the experiments and simulations. The relationship of κ to relative magnetic permeability is shown for each coating layer. The solid lines in the figure represent the simulation results. The results indicate that the enhancement of the coil inductance increased with an increase in the coating thickness, despite the material maintaining an identical magnetic permeability. A thicker coating enables greater magnetic flux penetration into the material, thereby reducing the reluctance and enhancing the inductance of the coil. κ exhibits nonlinear behavior regarding relative permeability, which can be represented by a second-order polynomial equation as follows.

$$\kappa = a\mu_{\mathrm{r}}^2 + b\mu_{\mathrm{r}} + c. \tag{23}$$

The parameters fitted to Eq. (23) based on the coating thickness is presented in Table 2, where κ' denotes the inductance ratio derived from the experimental results. By replacing κ' into Equation (23), the magnetic permeability can be derived inversely from the experimental measurements. The experimental findings are represented as markers in Fig. 6. The markers were positioned above the fitting line corresponding to each coating thickness. The relative permeability varied, despite the coating maintaining an identical volumetric fraction. This resulted from the variation in the homogeneity of the ferritic steel particles within the epoxy polymer. The orange box in the plot shows the magnitude of deviation in the relative permeability. Consequently, the experimentally measured relative permeability

was defined as the mean value of the magnetic permeability with respect to the coating thickness. The relative permeabilities were measured at 1.084, 1.233, and 1.6 for ferritic particle–epoxy polymer volumetric ratios of 0.0393, 0.0983, and 0.197, respectively. The experimentally obtained relative magnetic permeabilities were compared with those computed using the Maxwell–Garnett equation. The results of this comparison are presented in Fig. 10. The actual and calculated results exhibited similar values, indicating the feasibility of the experimental approach.

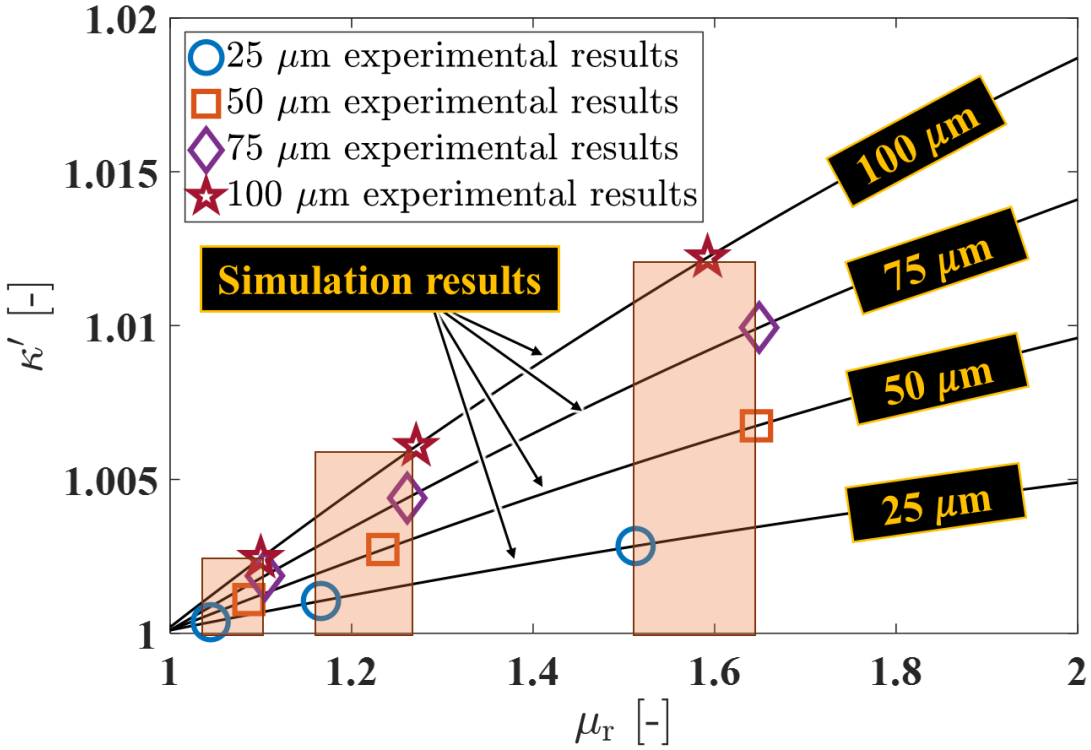


Fig. 9. Relative permeability prediction and validation

Table 2. Fitted parameters and experimental results of κ'

Thickness [μm]	Fitted parameter [-]	f [-]	κ'[-]
25	a_1: -0.0011	0.0393	1.000361
	b_1: 0.0081	0.0983	1.00105
	c_1: 0.9931	0.197	1.002837

50	a_2: -0.0022	0.0393	1.001099
	b_2: 0.0161	0.0983	1.002722
	c_2: 0.9862	0.197	1.006741
75	a_3: -0.0033	0.0393	1.00187
	b_3: 0.0239	0.0983	1.004395
	c_3: 0.9795	0.197	1.009939
100	a_4: -0.0044	0.0393	1.002444
	b_4: 0.0317	0.0983	1.006084
	c_4: 0.9729	0.197	1.012218

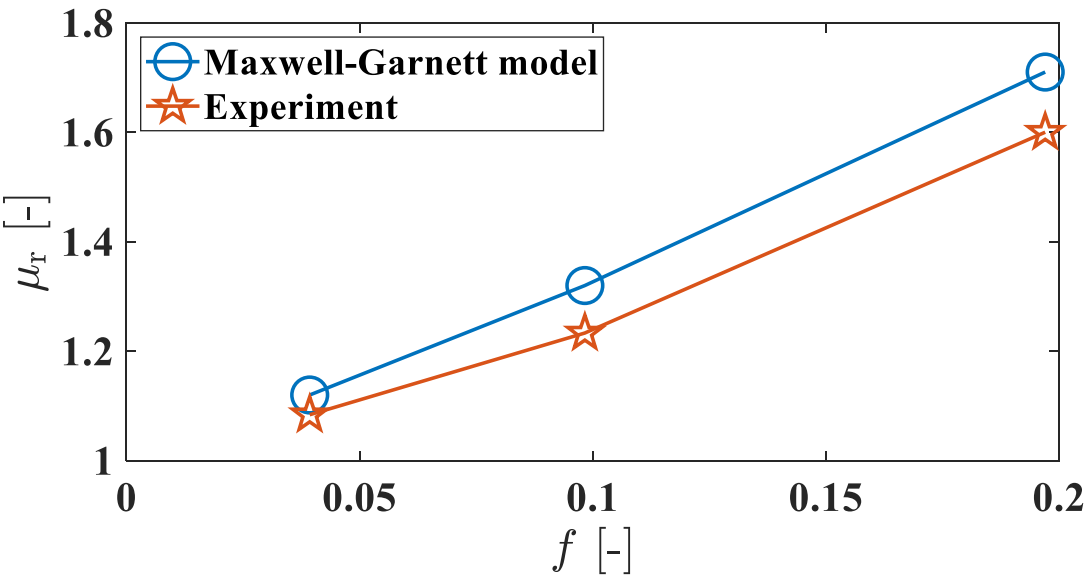


Fig. 10. Predicted and experimental values of relative permeability for magnetic coatings

As previously mentioned, the coating material must satisfy two objectives. The primary objective was the sensitivity of the electromagnetic sensor response, whereas the secondary objective was the adhesion properties. Numerical simulations were conducted to examine the response of the electromagnetic sensor in the presence of coating defects, as shown in Fig. 11. For realistic results, the geometries of the conductor and coating were set to match those of the actual ACCC. The aluminum

conductor was comprised of two layers, each with a thickness of 5 mm, with the coating located below. The relative magnetic permeabilities of the coatings were controlled at 1.084, 1.233, and 1.6, as determined experimentally. Additionally, the coating thickness was set at 25, 50, 75, and 100 μm, consistent with the prototypes. The electrical conductivity of the conductor was 36 MS/m, and no electromagnetic properties were assigned to the composite. A defect of 10 mm was created at the center along the length of the axis. The ECT simulation was performed utilizing 12 parameter combinations (magnetic permeability and thickness) with the designed electromagnetic sensor. The sensor was scanned along the length of the wire to observe variations in the absolute current of the pickup coil. The driving frequency was fixed at 100 Hz, and the absolute current value of the pickup coil was employed for fault detection.

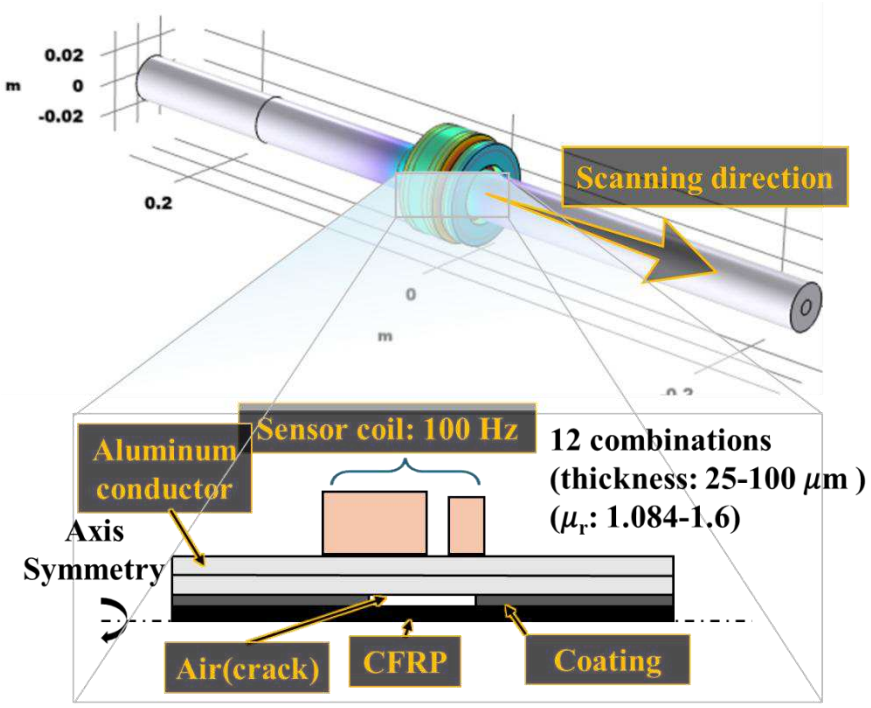
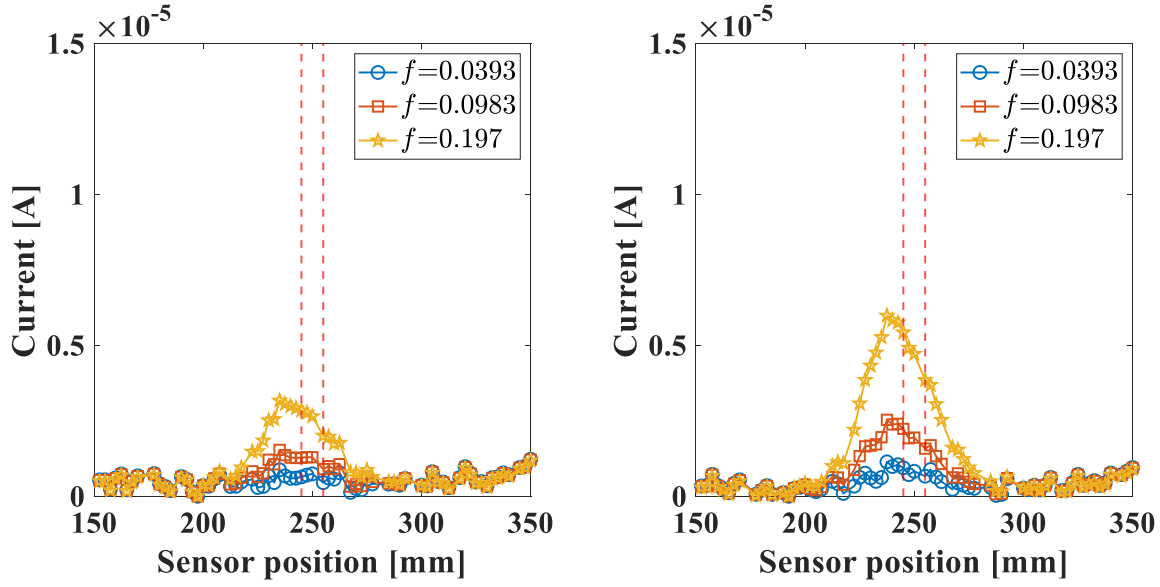


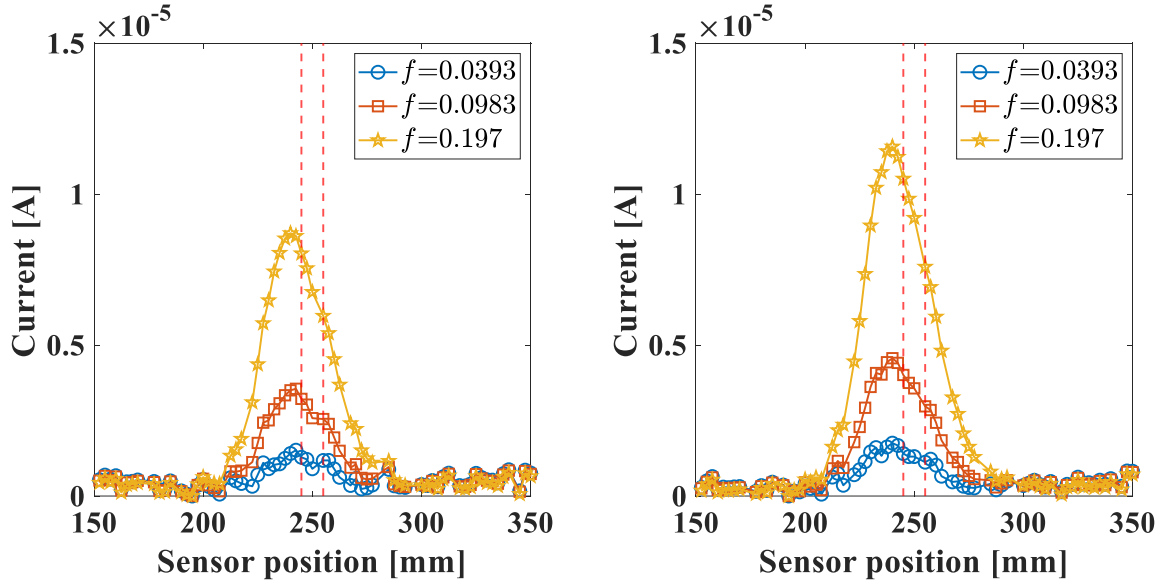
Fig. 11. Numerical simulation of electromagnetic method for ACCC inspection

The simulation results are presented in Fig. 12. Figures (12a)–(12d) present the results corresponding to coating thicknesses of 25, 50, 75, and 100 μm, respectively. Each figure indicates that the current from the pick-up coil varied with the volumetric ratio of the particles in the coating. The red dashed

lines denote the initial and final positions of the flaws in the simulation. The results indicated that the detection capability was enhanced with an increase in the volumetric ratio of the ferritic steel particles. Furthermore, the detected signal was amplified with increasing coating thickness, even when the volumetric ratio was maintained at a fixed level. The simulation results showed that both the thickness and volumetric ratio enhanced the detection sensitivity of the electromagnetic sensors. Undesirable noisy signals from defect-free areas hinder the identification of defect signals. Consequently, the SNR must be sufficiently high to identify flaws in the received signals. The SNR should exceed 10 dB to obtain reliable measurements (Department of the Air Force, 2014; Hughes et al., 2014). The coating material was optimized by adjusting the volumetric ratio and thickness to achieve a minimum SNR limit of 10 dB.



(a) (b)



(c) (d)

Fig. 12. Monitoring simulation results regarding to the coating thickness: (a) 25 mm, (b) 50 mm, (c) 75 mm and (d) 100 mm

Adhesion tests for the coating prototypes were performed according to the ASTM-3359 cross-cut tape standards (Goh et al., 2002; Magdaleno-López & de Jesús Pérez-Bueno, 2020). The coating was divided into 25 squares by cutting the surface into six vertical and horizontal lines. The lines were separated by 2 mm, and tape was attached to the surface. The tape was gradually removed after 90 s while ensuring that the pulling direction was as parallel to the surface as possible. The removal rate was determined by measuring the failed area of the coating. Adhesion levels were categorized into six grades, with each grade corresponding to a specific range in the detached area. The ASTM-3359 grades range from 6b to 0b, with lower numbers indicating poorer adhesion properties. All the test results for our prototype coatings were categorized as grades 3b to 0b. Grade 3b indicates a removal rate that varies from 5% to 15%. Grades 2b and 1b correspond to 15%–35% and 35%–65%, respectively. The lowest grade was 0b, which exhibited a removal rate of more than 65%.

The results of the adhesion experiments are presented in Fig. 13. Tests were performed on 12 prototype coating specimens, and the detached area was determined by capturing converted grey scale images. The failed region is indicated by white colors, which was accurately evaluated using MATLAB. The

results indicated that the removal rate increased with increasing thickness, even when the particle volumetric ratio remained constant. Moreover, the removal rate increased as the particle volumetric ratio increased while maintaining a fixed coating thickness. Coatings with weak adhesion properties can cause false alarms during electromagnetic testing of the ACCC and damage product reliability. Consequently, the particle volumetric ratio and coating thickness must be reduced to produce highly adhesive materials.

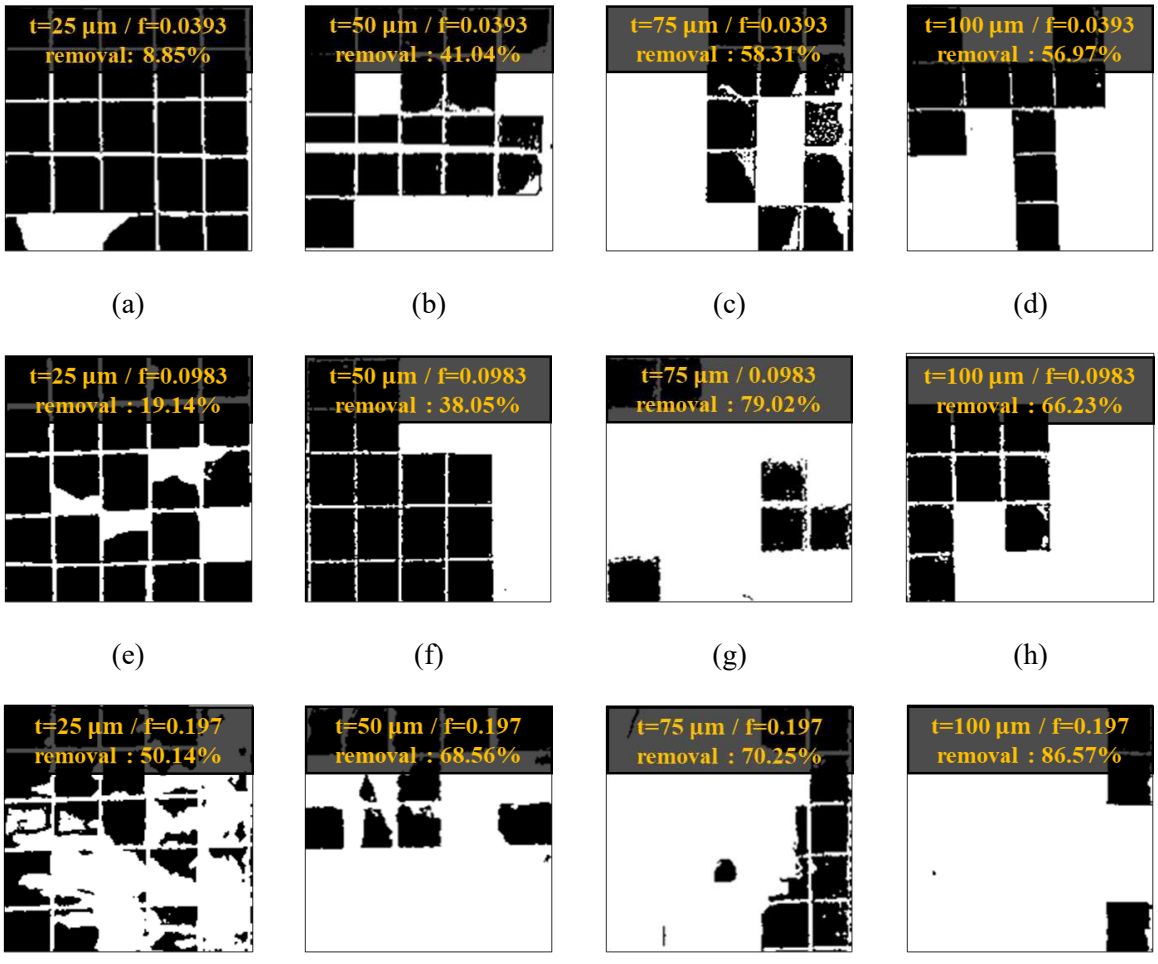


Fig. 13. Cross-cut test results of the magnetic coatings: (a) t=25 µm / f=0.0393, (b) t=50 µm / f=0. 0393, (c) t=75 µm / f=0. 0393, (d) t=100 µm / f=0. 0393, (e) t=25 µm / f=0.0983, (f) t=50 µm / f=0.0983, (g) t=75 µm / f=0.0983, (h) t=100 µm / f=0.0983, (i) t=25 µm / f=0.197, (j) t=50 µm / f=0.197, (k) t=75 µm / f=0.197 and (l) t=100 µm / f=0.197

Defect simulations and adhesion tests indicated that the particle volumetric ratio and thickness must be optimized to enhance the electromagnetic sensor response and reduce the removal rate. The sensor response, characterized by the SNR, exhibits a trade-off with the adhesion properties. Consequently, the property can be optimized using the multi-objective problem as follows (Gopakumar et al., 2018).

$$\text{minimize} \quad F = \{f_1(x_1, x_2), f_2(x_1, x_2)\} \tag{18a}$$

$$\begin{aligned} \text{subject to} \quad & f_1(x_1, x_2) \leq -10 \\ & f_2(x_1, x_2) \leq 0.65 \\ & 0.01 \leq x_1 \leq 0.2 \\ & 10 \leq x_2 \leq 100 \end{aligned} \tag{18b}$$

where f_1 is the objective function representing the negative SNR, and f_2 signifies the coating removal rate. x_1 and x_2 represent the volumetric ratio of the particles and thickness of the coating, respectively. The SNR is converted to a negative value owing to the dependence of most optimization algorithms on the gradient descent method, which seeks to minimize the objective function. The constraints of the objective functions are presented in Equation (18b). The general SNR required for dependable defect identification is 10 dB. We can also assume that the maximum removal should not exceed 65%, thereby preventing the lowest rating in the adhesion test.

Two objective functions were established based on the particle volumetric ratio and coating thickness for the optimization procedure. The SNR function was fitted using linear regression, whereas the removal rate function was fitted using a two-variable nonlinear function as follows:

$$f_1 = \beta_1 x_1 + \beta_2 x_2 - \beta_3, \tag{19a}$$

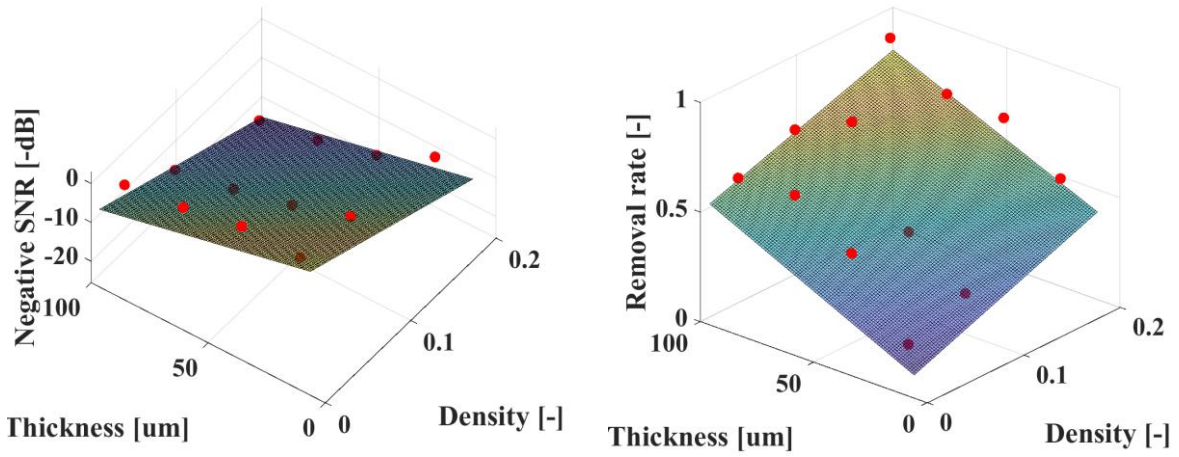
$$f_2 = \gamma_1 x_1 + \gamma_2 x_1^{\gamma_3} + \gamma_4 x_2 + \gamma_5 x_2^{\gamma_6} + \gamma_7 x_1 x_2 \tag{19b}$$

where β and γ represent the model parameters for the objective functions. Each function parameter was estimated using the least-squares method to minimize the difference between the predicted and experimental results. Table 3 presents the parameters of the fitted model. The fitted objective functions are shown in Fig. 14. The experimental data are represented by the red markers in the images, demonstrating that the fitted functions aligned closely with the experimental results.

473 Table 3. Fitting parameters for objective functions

Objective function	Parameters	Value	Unit
f_1	β_1	-86.68	[-]
	β_2	-0.1311	
	β_3	5.193	
f_2	γ_1	1.763	[-]
	γ_2	19.53	
	γ_3	51.02	
	γ_4	-0.155	
	γ_5	0.16	
	γ_6	1.00	
	γ_7	-0.00245	

474



(a) (b)

Fig. 14. Fitted models of the objective function: (a) negative SNR and (b) adhesion rate

475

476 To achieve durability in the magnetic coating structure and simultaneously enhance the fracture
477 detection capability, the volumetric ratio and thickness can be adjusted by minimizing both objective

functions, as shown in Eq. (19). The complete solutions for the objective functions within the specified ranges of x_1 and x_2 are represented by the black circles in Fig. 15. The x-axis denotes f_1, and the y-axis denotes f_2. The constraints for the objective functions are shown by a red dashed line, indicating values below -10 for negative SNR and below 0.65 for the removal rate. The entire solution appears as a rotated parallelogram, with vertices at the far ends representing the extreme ends of the solutions. The farthest point on the line perpendicular to the vertices is the knee point, which represents the optimal solution. The optimal solution occurred at an SNR of 13.45 dB and a removal rate of 0.4. The magnetic coating property yielding the most comparable result to the ideal solution was a thickness of 50 um and a volumetric ratio of 0.0983. The SNR and removal rate of the chosen coating were 11.05 dB and 0.38, respectively. Consequently, the coating was developed with the specified thickness and volumetric ratio.

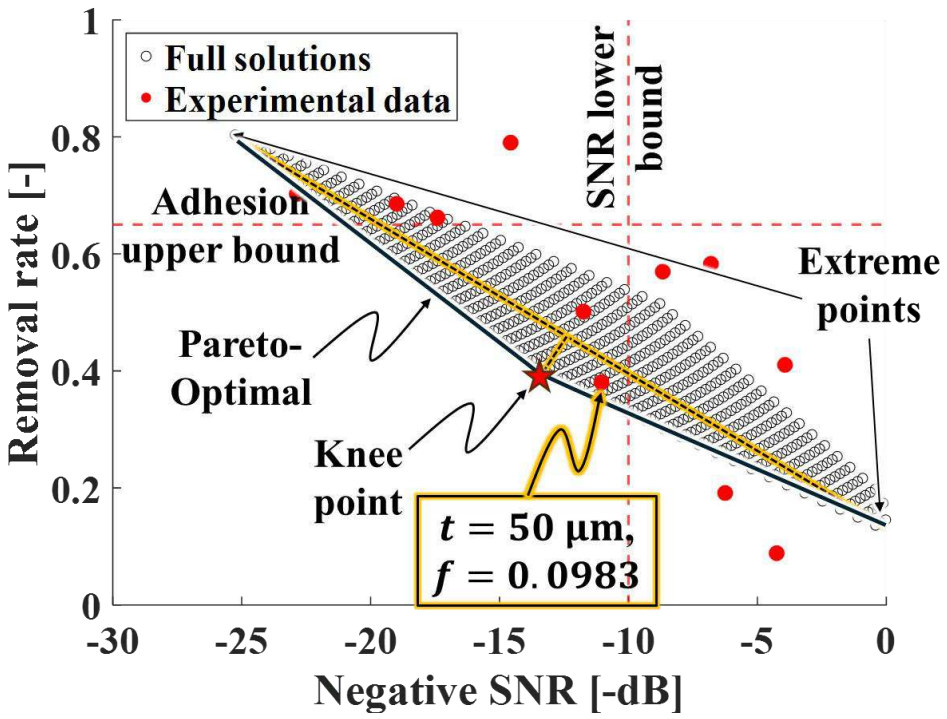
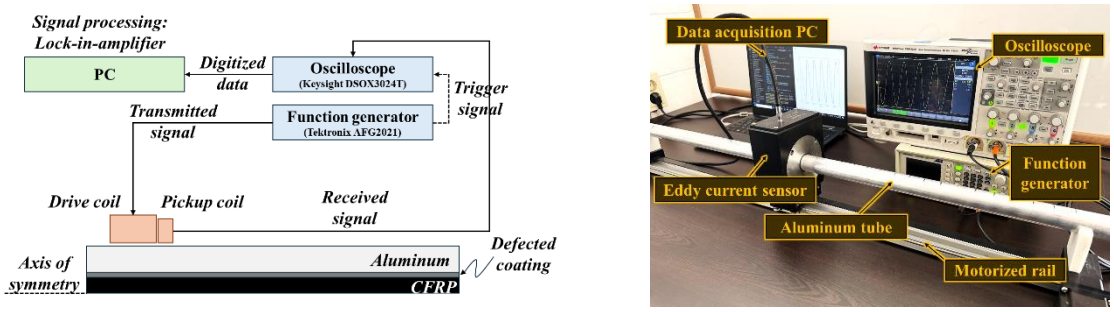


Fig. 15. Optimized point for the magnetic coating regarding to objective functions

5. Validation of the inspection method

An experiment was conducted to validate the magnetic coating and electromagnetic field testing

methods for detecting faults in composite cores of ACCCs. The magnetic coating was applied to the composite core surface according to the optimal specifications. A crack of 80 mm was intentionally induced at the center of the specimen along the longitudinal axis. The specimen consisted of an 800 mm aluminum tube with a thickness of 9 mm, potentially representing the conductor part in the ACCC. The cracked magnetically coated composite core was inserted into an aluminum tube. The fabricated electromagnetic sensor was affixed to a stage motor and the conductor was monitored at a speed of 20 mm/s. An alternating current was applied to the drive coil of the electromagnetic sensor using a function generator (Tektronix AFG2021) at a frequency of 100 Hz. The pickup coil received the signal, which was digitized using a Keysight DSOX3024T oscilloscope and subsequently processed using a PC. The hardware was managed using Python software, which gathers data in real time. The real and imaginary components were analyzed using the lock-in amplifier (LIA) technique, which accurately detected impedance variations (Chen et al., 2021; Meng et al., 2023; Zhang et al., 2024). The whole configuration of the experiment is shown in Fig. 16.

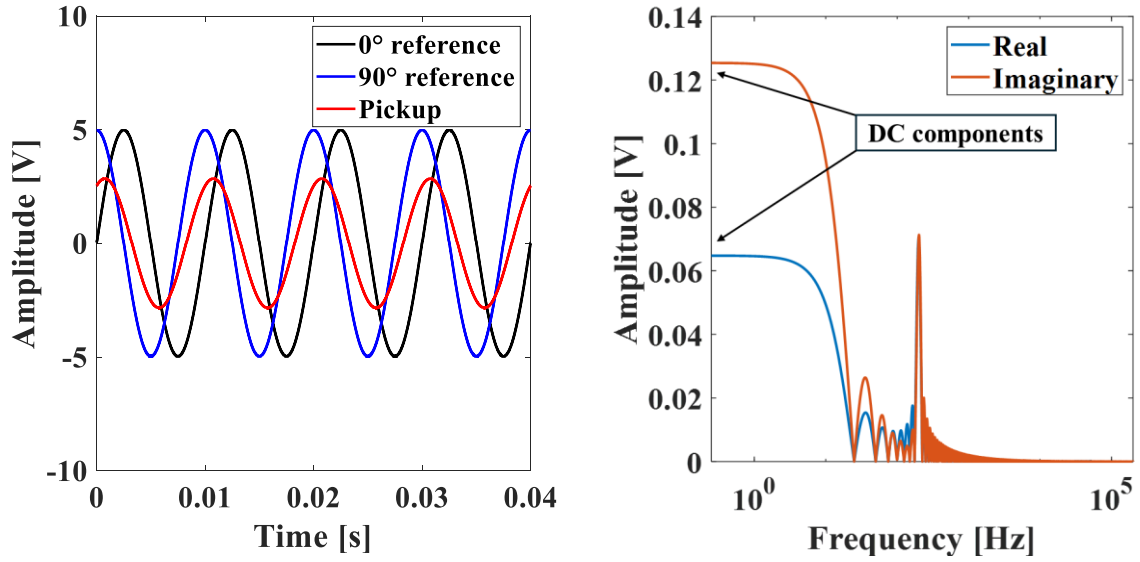


(a) (b)

Fig. 16. Electromagnetic field based inspection experiment setup for ACCC: (a) schematic of the setup and (b) picture of the entire experimental setup

The pickup coil receives signals in a sinusoidal form. The LIA method processes this signal by utilizing reference signals that are input into the driving coil. The reference signals comprised the original signal and a signal with a 90-degree phase delay. In the LIA approach, the DC components of the original and phase-delayed signals correspond to the real and imaginary parts, respectively. The advantage of this method is its ability to accurately detect small phase changes even in the presence of noise within the received signal. The details of the signal processing technique have been described in

a previous study (Shim et al., 2025). Figure 17 depicts the received and processed signals. Figure 9b shows a peak at 0 Hz, which indicates the presence of real and imaginary components. This study used the overall amplitude of the signal for flaw identification.



(a) (b)

Fig. 17. Frequency analysis of LIA signal processing method: (a) received and reference signals and (b) real and imaginary parts of the received signal

Figure 18 shows the results of electromagnetic field testing of the aluminum pipe. The relative amplitude values were presented with the minimum data point adjusted to zero. The data points within the non-defective region exhibited noise, potentially caused by the inhomogeneity of the magnetic coating. The data points were interpolated and smoothed using a positional step of 0.1 mm for enhanced visibility. The interpolated data are represented by black lines. The flaw was located 400 mm from the starting point as detected by an electromagnetic sensor. The sensor identified a defect in the core despite the aluminum conductor being attached externally to the composite core. The SNR of the flawed signal was determined to be 11.9 dB, which agreed closely with the design value. The experimental results indicated that the magnetic coating can identify faults in the composite core of ACCCs using an electromagnetic sensor that exhibits a favorable SNR and an acceptable removal rate.

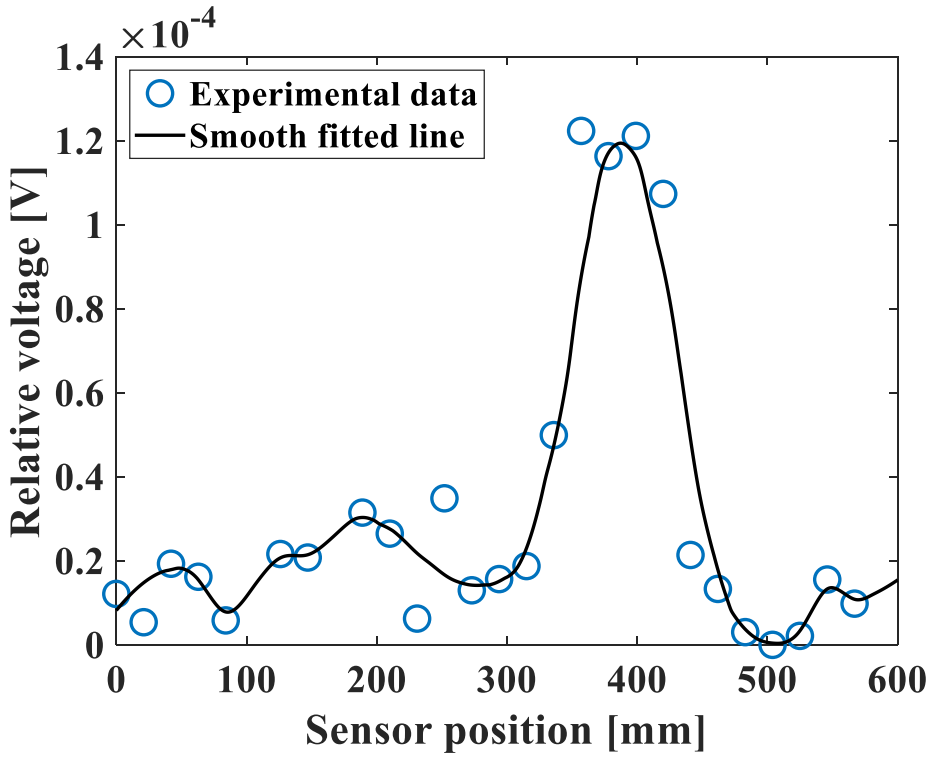


Fig. 18. Relative voltage of the electromagnetic field testing of ACCC

6. Conclusions

This paper introduces a magnetic coating interlayer and an electromagnetic monitoring approach for detecting cracks in ACCC composite cores. Conventional inspection methods are challenging to apply because the objective is to inspect defects in the inner composite core of an ACCC surrounded by two aluminum conductors. To address this problem, we developed a magnetic coating material to increase the magnetic permeability of a composite core surface. Additionally, a sensor was designed to detect changes in the electromagnetic field caused by defects in the inner core from the exterior of the ACCC. Theoretical analysis revealed that the alteration in the induced current was optimized when the ACCC was subjected to an electromagnetic field with a frequency of approximately 100 Hz. Consequently, an electromagnetic sensor was designed and manufactured to generate a specified frequency. To specify the fabrication of the magnetic coating, we optimized the volumetric ratio of ferritic steel particles in the coating and the coating thickness by evaluating the SNR of the defect signals and the adhesive strength of the coating. Numerical simulations were performed to examine signal alterations in the

presence of an artificial flaw within the composite core. A cross-cut test was subsequently conducted to evaluate the adhesion levels. Pareto-front analysis was employed to identify the optimal solution from a comprehensive collection of objective function solutions. The optimum solution was found to be a coating thickness of 50 mm and a volumetric particle ratio of 0.093, resulting in an SNR of 13.45 and a removal rate of 0.4. This solution satisfied the established criteria (SNR > 10 dB and removal rate < 0.65) for the optimization problem. An inspection using an electromagnetic field was performed on an aluminum pipe with a defective magnetically coated composite core at its center. The proposed approach exhibited strong detection capability with an SNR of 11.9 dB in this configuration. Consequently, the proposed method provides a reliable approach for identifying defects in the composite core of ACCCs and is suitable for both pre-installation inspection and in-service maintenance.

ACKNOWLEDGMENT

This work was supported by LS Cable & System Ltd. and the Technology Innovation Program (RS-2025-25447560) funded by the Ministry of Trade, Industry & Energy (MOTIE, Korea)

References

Alawar, A., Bosze, E. J., & Nutt, S. R. (2005). A Composite Core Conductor for Low Sag at High Temperatures. *IEEE Transactions on Power Delivery*, *20*(3), 2193–2199. https://doi.org/10.1109/TPWRD.2005.848736

Burks, B., Armentrout, D., & Kumosa, M. (2010). Failure prediction analysis of an ACCC conductor subjected to thermal and mechanical stresses. *IEEE Transactions on Dielectrics and Electrical Insulation*, *17*(2), 588–596. https://doi.org/10.1109/TDEI.2010.5448116

Chang, H.-M., & Liao, C. (2011). A Parallel Derivation to the Maxwell-Garnett Formula for the Magnetic Permeability of Mixed Materials. *World Journal of Condensed Matter Physics*, *01*(02), 55–58. https://doi.org/10.4236/wjcmp.2011.12009

Chen, X., Wei, M., Chen, K., & Li, S. (2021). Research on weak signal detection of integral average digital lock-in amplifier. *Measurement Science and Technology*, *32*(10), 105905. https://doi.org/10.1088/1361-6501/ac0d74

Department of the Air Force. (2014). *NONDESTRUCTIVE INSPECTION METHODS, BASIC THEORY (TO 33B-1-1, NAVAIR 01-1A-16-1, TM 1-1500-335-23)*.

Goh, L. L. N., Toh, S. L., Chooi, S. Y. M., & Tay, T. E. (2002). Adhesion measurement of thin films to a porous low dielectric constant film using a modified tape test. *Journal of Adhesion Science and*

Technology, *16*(6), 729–744. https://doi.org/10.1163/156856102760099906

Gopakumar, A. M., Balachandran, P. V., Xue, D., Gubernatis, J. E., & Lookman, T. (2018). Multi-objective Optimization for Materials Discovery via Adaptive Design. *Scientific Reports*, *8*(1), 3738. https://doi.org/10.1038/s41598-018-21936-3

Hu, Y., He, N., Xie, L., Chen, D., Gao, C., & Ding, H. (2024). Improved automatic defect detection from X-ray scans for aluminum conductor composite core wire based on modified Skip-GANomaly. *NDT and E International*, *143*. https://doi.org/10.1016/j.ndteint.2024.103050

Hu, Y., Wang, J., Zhu, Y., Wang, Z., Chen, D., Zhang, J., & Ding, H. (2021). Automatic defect detection from X-ray Scans for Aluminum Conductor Composite Core Wire Based on Classification Neutral Network. *NDT and E International*, *124*. https://doi.org/10.1016/j.ndteint.2021.102549

Hughes, R., Fan, Y., & Dixon, S. (2014). Near electrical resonance signal enhancement (NERSE) in eddy-current crack detection. *NDT & E International*, *66*, 82–89. https://doi.org/10.1016/j.ndteint.2014.04.009

Jackson, J. D. (1998). *Classical electrodynamics* (3rd ed.). Wiley.

Jalilian, M., Riba, J.-R., & Parvizi, P. (2024). Aluminum Conductor Steel-Supported Conductors for the Sustainable Growth of Power Line Capacity: A Review and Discussion. *Materials*, *17*(18), 4536. https://doi.org/10.3390/ma17184536

Jeong, S., Kim, M.-G., Kim, J.-H., & Oh, K.-Y. (2023). Thermal monitoring of live-line power transmission lines with an infrared camera mounted on an unmanned aerial vehicle. *Structural Health Monitoring*, *22*(6), 3707–3722. https://doi.org/10.1177/14759217231156359

Kim, J., Kim, C., Shim, Y.-D., & Lee, E.-H. (2025). Investigation of Plastic Deformation and Electromagnetic Interaction for Copper Losses Caused by Hairpin Motor Manufacturing. *IEEE Transactions on Transportation Electrification*, 1–1. https://doi.org/10.1109/TTE.2025.3549447

Larsson, R., Brambati, G., & Gutkin, R. (2023). Compressive failure and kink-band formation modeling. *European Journal of Mechanics - A/Solids*, *99*, 104909. https://doi.org/10.1016/j.euromechsol.2023.104909

Lee, E.-H. (2021). A model for irreversible deformation phenomena driven by hydrostatic stress, deviatoric stress and an externally applied field. *International Journal of Engineering Science*, *169*, 103573. https://doi.org/10.1016/j.ijengsci.2021.103573

Lee, E.-H. (2024). Relativistic constitutive modeling of inelastic deformation of continua moving in space-time. *Communications in Nonlinear Science and Numerical Simulation*, *131*, 107821. https://doi.org/10.1016/j.cnsns.2024.107821

Lequien, F., Auzoux, Q., Moine, G., Rousseau, M., Pasquier-Tilliette, S., Holande, A., Ammi, S., Heurtault, S., & Prieur, P. (2021). Characterization of an aluminum conductor steel reinforced (ACSR) after 60 years of operation. *Engineering Failure Analysis*, *120*, 105039. https://doi.org/10.1016/j.engfailanal.2020.105039

Li, Z., Wang, Q., Zhang, T., Ju, C., Suzuki, S., & Namiki, A. (2023). UAV High-Voltage Power Transmission Line Autonomous Correction Inspection System Based on Object Detection. *IEEE Sensors Journal*, *23*(9), 10215–10230. https://doi.org/10.1109/JSEN.2023.3260360

Liao, C., Yi, Y., Chen, T., Cai, C., Deng, Z., Song, X., & Lv, C. (2022). Detecting Broken Strands in Transmission Lines Based on Pulsed Eddy Current. *Metals*, *12*(6). https://doi.org/10.3390/met12061014

Liu, Y., Tian, G., Gao, B., Lu, X., Li, H., Chen, X., Zhang, Y., & Xiong, L. (2022). Depth quantification of rolling contact fatigue crack using skewness of eddy current pulsed thermography in stationary and scanning modes. *NDT & E International*, *128*, 102630. https://doi.org/10.1016/j.ndteint.2022.102630

Liu, Z., Wu, G., He, W., Fan, F., & Ye, X. (2022). Key target and defect detection of high-voltage power transmission lines with deep learning. *International Journal of Electrical Power and Energy Systems*, *142*. https://doi.org/10.1016/j.ijepes.2022.108277

Magdaleno-López, C., & de Jesús Pérez-Bueno, J. (2020). Quantitative evaluation for the ASTM D4541-17/D7234 and ASTM D3359 adhesion norms with digital optical microscopy for surface modifications with flame and APPJ. *International Journal of Adhesion and Adhesives*, *98*, 102551. https://doi.org/10.1016/j.ijadhadh.2020.102551

Mahin, A. U., Islam, S. N., Ahmed, F., & Hossain, Md. F. (2022). Measurement and monitoring of overhead transmission line sag in smart grid: A review. *IET Generation, Transmission & Distribution*, *16*(1), 1–18. https://doi.org/10.1049/gtd2.12271

Mazzeschi, M., Nuñez, K. C., Cañibano, E., & Merino, J. C. (2023). Monitoring of thermoplastic induction welding defects. Use of electromagnetic properties as a predictive tool. *Structural Health Monitoring*, *22*(3), 1613–1627. https://doi.org/10.1177/14759217221111979

Meng, Z., He, X., Li, Y., Huang, J., Chen, D., & Wang, Z. (2023). A Multi-Contaminants Detection Sensor Based on Digital Lock-In Amplifier Module With High Sensitivity and High Detectability. *IEEE Sensors Journal*, *23*(14), 16123–16135. https://doi.org/10.1109/JSEN.2023.3282277

Park, J.H., Park, H., Kim, T., Kim, J., Lee, E-H. (2024). Numerical analysis of thermal and mechanical characteristics with property maps in complex semiconductor package designs, *Applied Mathematical Modelling*, 130, 140-159.

Shim, Y.-D., Kim, C., Kim, J., Yoon, D.-H., Yang, W., & Lee, E.-H. (2025). Integrated modeling framework for the interactions of plastic deformation, magnetic fields, and electrical circuits: Theory and applications to physics-informed real-time material monitoring. *International Journal of Plasticity*, *184*, 104212. https://doi.org/10.1016/j.ijplas.2024.104212

Sihvola, A. (1999). *Electromagnetic Mixing Formulas and Applications*. Institution of Engineering and Technology. https://doi.org/10.1049/PBEW047E

Sim, J.-W., Kim, T.-H., Kang, N., Lee, H. J., & Lee, E.-H. (2024). Effective thermo-electric-mechanical modeling of capacitively coupled plasma in low-pressure conditions: Modeling and application in dry etching. *Applied Mathematical Modelling*, *127*, 32–59. https://doi.org/10.1016/j.apm.2023.11.021

Sun, H., Wang, T., Liu, Q., Wang, Y., & Qing, X. (2021). A two-dimensional eddy current array–based sensing film for estimating failure modes and tracking damage growth of bolted joints. *Structural Health Monitoring*, *20*(3), 877–893. https://doi.org/10.1177/1475921719843062

Trung, L. Q., Kasai, N., Le, M., Sekino, K., & Funada, Y. (2024). Crack detection using a cutting-edge flexible eddy current sensor with voltage and phase measurement techniques. *Mechanical Systems and Signal Processing*, *219*, 111613. https://doi.org/10.1016/j.ymssp.2024.111613

Wang, F., Song, G., Mao, J., Li, Y., Ji, Z., Chen, D., & Song, A. (2023). Internal Defect Detection of Overhead Aluminum Conductor Composite Core Transmission Lines With an Inspection Robot and Computer Vision. *IEEE Transactions on Instrumentation and Measurement*, *72*. https://doi.org/10.1109/TIM.2023.3265104

Wheeler, H. A. (1942). Formulas for the Skin Effect. *Proceedings of the IRE*, *30*(9), 412–424. https://doi.org/10.1109/JRPROC.1942.232015

Xia, Y., Jiang, X., Zhang, Z., Hu, J., & Sun, C. (2013). Detecting broken strands in transmission line - Part 1: Design of a smart eddy current transducer carried by inspection robot. *International Transactions on Electrical Energy Systems*, *23*(8), 1409–1422. https://doi.org/10.1002/etep.1669

Xu, C., Li, Q., Zhou, Q., Zhang, S., Yu, D., & Ma, Y. (2022). Power Line-Guided Automatic Electric Transmission Line Inspection System. *IEEE Transactions on Instrumentation and Measurement*, *71*. https://doi.org/10.1109/TIM.2022.3169555

Zhang, Q., Jeong, W., & Kang, D. J. (2024). Lock-in amplifiers as a platform for weak signal measurements: Development and applications. *Current Applied Physics*, *66*, 95–109. https://doi.org/10.1016/j.cap.2024.07.002